B-scan imaging and thermal lesion monitoring using miniaturized dual-functionality ultrasound arrays

Inder Raj S. Makin, T. Douglas Mast,
Waseem Faidi, and Megan Runk
Ethicon Endo-Surgery, 4545 Creek Rd., Cincinnati OH 45242
Email: mast@iglou.com

Peter G. Barthe and Michael H. Slayton
Guided Therapy Systems
33 S. Sycamore St., Mesa AZ 85202
Email: p.barthe@guidedtherapy.com

***Abstract*— A key potential advantage for ultrasound therapy is the ability to treat and image tissue using the same device. Recent development of miniaturized dual-functionality (image and treat) probes, capable of both high power (*e.g.*, > 80 W/cm^2 at 3.1 MHz) and broad bandwidth (*e.g.*, 50% centered at 3.5 MHz), has allowed real-time imaging and monitoring of thermal lesioning with complete co-registration of image and treatment regions of interest. Using arrays with 32 elements spanning an aperture of 2.3×48 mm and center frequencies of about 3.5 MHz, high-quality B-scan images and useful monitoring information can be obtained during therapy planning and treatment.**

B-scan image quality is quantitatively comparable to current transabdominal ultrasound arrays (azimuthal point resolution 3 mm, axial point resolution 2 mm, contrast resolution 3 dB). Challenges associated with limited probe dimensions and channel count are met using interpolation, filtering, and reverberation reduction methods that improve image definition and contrast. Tissue boundaries and critical structures are shown to be clearly delineated in phantoms and *in vivo*.

Monitoring of thermal lesioning by these arrays can be performed simultaneously using the same array elements. In addition to real-time B-scan visualization, techniques employed include quantification of tissue backscatter and attenuation changes, and analysis of echo waveform changes to detect boiling and tissue modification. Gas activity, associated with gross B-scan changes as well as large waveform and attenuation changes, consistently implies tissue ablation for the exposure conditions studied here. However, preliminary experience suggests that absence of large echo changes does not consistently predict absence of ablation, and that the magnitude of echo changes shows limited correlation with the severity of ablation.

I. Introduction

Thermal ablation using intense ultrasound is a therapy with potential utility for treatment of pathological soft tissues [1]. For many applications, such as cancer treatment, a goal of thermal ablation treatments is to reliably cause thermal necrosis in a relatively large tissue volume (*e.g.*, greater than 5 cm diameter including a safety margin) [2]. In current practice, thermal destruction of large tissue volumes is most commonly performed using (electromagnetic) radiofrequency ablation [2].

Intense ultrasound treatment, first proposed in the 1950's [3], has the potential advantages of selectivity, integrated image guidance, and a noninvasive or minimally invasive approach. To date, most effort in this area has concentrated on extracorporeal or intracavitary high-intensity focused ultrasound (HIFU) [1]. An alternative approach, which can allow faster ablation of large tissue volumes at the expense of minimal invasiveness, is thermal coagulation using miniaturized ultrasound transducers that can be deployed laparoscopically or interstitially [4]. Recent developments in transducer technology have allowed the construction of interstitial linear arrays capable of both intense ultrasound treatment and B-scan imaging [4], [5].

In the work presented here, miniaturized dual-functionality (image and treat) ultrasound arrays have been used to investigate bulk ablation of soft tissue with simultaneous B-scan imaging and monitoring. A significant advantage of this approach, as opposed to use of separate transducer elements for imaging and therapy, is that the imaged region of tissue is exactly co-registered with the treatment region, regardless of any uncertainties in the treatment geometry or the acoustic properties of the tissue. Compared to other minimally invasive ablation modalities for liver such as RF ablation, the current approach offers better selectivity of treatment as well as better predictability of tissue ablation due to the imaging and monitoring capabilities of the probes employed.

II. Methods

Miniaturized image-treat ultrasound arrays, with center frequencies between 3–8 MHz, 16–64 elements, pulse-echo bandwidths of 50%–70%, and package diameters of 3–10 mm, have been developed. Array pitches range from 1 to 3 wavelengths at the array center frequencies, so that focusing and imaging are feasible. When driven at resonance with high power for thermal therapy, these arrays are typically capable of surface power densities up to 80 W/cm^2. The array technology, as well as the electronic system used to control the arrays for imaging and therapy, are described elsewhere [4], [5].

Ablation and imaging experiments for these arrays were performed using excised porcine liver tissue. *In vitro* experiments were performed at room temperature in a water tank. *In vivo* ablation experiments were performed using a porcine animal model in surgical procedures performed after a laparotomy. Upon completion of ablation experiments, tissue specimens were frozen, sliced into ∼3 mm sections using a standard meat slicer, and digitally photographed for quantitative evaluation of thermal lesion dimensions, including ablation depth, volume, and rate.

0-7803-8412-1/04/$20.00 (c)2004 IEEE.

2004 IEEE International Ultrasonics, Ferroelectrics, and Frequency Control Joint 50th Anniversary Conference

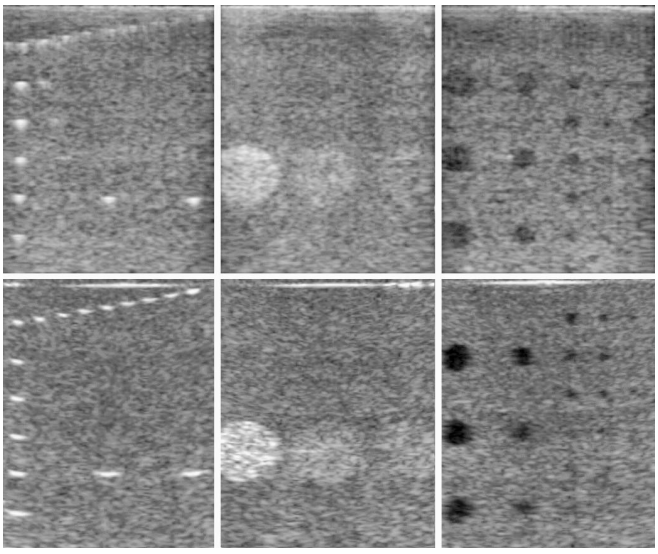

Fig. 1. Reference phantom images of 0.12 mm nylon wire targets, 15 mm grayscale targets of contrast 15, 6, and 3 dB above background, and anechoic cysts of diameter 8, 6, 4, 3, and 2 mm. Each plot shows a region of area 49 mm in width and 73 mm in height. Top row: 3 MHz, 32 element miniaturized image-treat array. Bottom row: 3.5 MHz, 128 element curved linear array with 3 cm standoff.

In all experiments, B-scan imaging was performed in real time by the controlling electronics. Enhanced B-scan images were also formed by synchronously sampling the RF output of the imaging module at a rate of 33 MHz using an analog-to-digital converter board (Gage Compuscope 1450) housed in a separate PC. The digitized A-line signals were decimated to a sampling rate of 11 MHz, bandpass filtered to result in a center frequency of 4.0 MHz and a 17.5% bandwidth, and coherently interpolated between adjacent signals to increase the effective line density.

In addition, an adaptive reverberation reduction method [6] was employed to reduce signal artifacts. In this method, the artifactual portion of the echo signals was assumed to be the portion that changes very slowly from frame to frame, while the overall echo signals may change substantially (*e.g.*, due to tissue motion). This approach is effective in removing ringdown artifacts that depend only on the probe geometry and the electronic characteristics of each channel. Artifacts were estimated using the formula

$$\begin{aligned} B(y,z,T_i) &\approx (1-\epsilon)\,p(y,z,T_{i-1}) + \epsilon\,p(y,z,T), \\ \epsilon &= \frac{\epsilon_0}{2\pi}\cos^{-1} r[p_{i-1},p_i] \end{aligned} \quad (1)$$

where $p(y,z,T_i)$ is the ith frame of RF echo data, ϵ is a weighting factor determined from the correlation coefficient r between a portion of two adjacent frames, and ϵ_0 is an user-definable coefficient less than unity. The estimated artifacts $B(y,z,T_i)$ were then digitally subtracted from the RF signals for each frame before envelope detection, logarithmic compression, scan conversion, smoothing, and display.

Image quality was evaluated using B-scan images of a standard quality assurance reference phantom (Model 539, ATS Laboratories). Postprocessed (filtered, smoothed, and reduced reverberation as described above) images were obtained using three representative 32 element, 3 MHz, 3 mm arrays, all of which showed comparable results. For comparison, analogous images were also obtained using a 128 element curved linear array transducer designed for transabdominal imaging with a center frequency of 3.5 MHz. To mimic the situation of transabdominally guided intervention, a 3 cm depth absorbing and scattering standoff, made of the same urethane material as the phantom background, was employed.

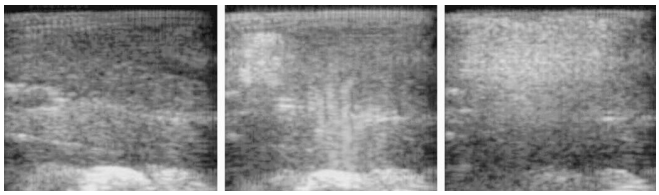

Fig. 2. B-scan images obtained from a 3 mm, 3 MHz, 32 element image-treat array during an *in vivo* interstitial ablation procedure in porcine liver. Each panel has width 49 mm and height 43 mm. Left to right: image before treatment, image after 60 s treatment showing initial hyperechoic region, image after 80 s treatment showing a broad hyperechoic region.

Monitoring using these arrays is performed in part using real-time B-scan imaging during therapy. In many cases, gas generation associated with tissue boiling causes bright (hyperechoic) regions to appear on B-scans, with corresponding distal darkening of the images due to increased attenuation. A simple monitoring method that quantifies these changes is performed by mapping changes in echo energy as a function of azimuthal position at specific depth ranges. This method is equivalent to reflex transmission imaging [7], which has been previously employed for monitoring of thermal therapy using conventional imaging transducers [8].

In addition to changes in echo energy, real-time B-scans during therapy indicate apparently random changes in echo signals associated with lesioning. These changes are greatest in hyperechoic regions presumably associated with tissue boiling, but can also be observed in isoechoic regions. Causes for these signal variations may include gas activity, structural changes due to ablation, and speckle motion due to acoustic streaming, radiation force, and thermal expansion. These signal changes can be quantified by integrating changes in echo energy over time, using a method [9] described by the formula

$$\begin{aligned} D(y,z,T_n) &= \frac{1}{n}\Big[\sum_1^n \iint w(y-\eta,z-\zeta)\,|p(\eta,\zeta,T_i) \\ &- p(\eta,\zeta,T_{i-1})|^2\,d\eta\,d\zeta\Big] / \langle |p(y,z,\tau)|^2 \rangle, \end{aligned} \quad (2)$$

where D is a cumulative measure of changes in echo signals, w is a smoothing window, typically several mm in diameter, p is the set of RF echo signals for frames obtained at instants T_i, and $\langle |p|^2 \rangle$ is the mean-square amplitude of the RF echo signals for one frame. The echo difference between adjacent frames closely spaced in time (limited by the achievable frame rate, which can be up to 200 fps depending on channel count) is squared, integrated spatially, and summed over n

frames to reduce random variations. This method is related to "turbulence" measures employed in color Doppler imaging [10] as well as qualitative assessment of large fluctuations in the Doppler signal, which has been investigated for monitoring of thermal ablation [11].

III. Results

For each probe, images of phantom regions demonstrating point resolution, contrast, and functional resolution (*i.e.*, resolution of small anechoic structures) are depicted in Fig. 1. Relative to the transabdominal probe, the 3 mm image-treat probe achieves superior point resolution in the azimuth (horizontal) direction, comparable point resolution in the range (vertical) direction, and comparable contrast and functional resolution.

B-scan images taken using a 3 MHz, 32 element, 3 mm image-treat probe during an *in vivo* interstitial ablation experiment are shown in Fig. 2. The exposure was performed by firing 24 elements (active aperture size 2.3×24 mm) with a total acoustic power of 69 W and a duty cycle of 80% (4 s therapy on, 1 s imaging only) for 18 cycles. The images shown were obtained in real time using the postprocessing methods described above including A-line interpolation and adaptive artifact reduction using Eq. (1).

The pre-treatment image shows resolution of liver structure including a large vessel. Typical effects of ablation on B-scan images are shown in the following two panels. The second panel shows a hyperechoic spot immediately after its spontaneous formation about 60 s after the beginning of treatment. The third panel shows the hyperechoic spot after about 80 s treatment, at which time the proximal portion of the image is dominated by the hyperechoic spot. Hyperechoic spots of this kind were found to occur in multiple *in vivo* and *ex vivo* experiments using image-treat probes, and consistently indicated significant tissue ablation. However, significant thermal lesioning was also found to sometimes occur in the absence of hyperechoic changes to the real-time B-scans.

B-scan images obtained during an *ex vivo* ablation experiment on porcine liver are shown in Fig. 3 together with plots of echo energy analogous to reflex transmission images. This experiment employed a single rectangular element, unfocused 4.7 MHz therapy transducer and a separate miniaturized imaging transducer (10 mm diameter, 128 elements, active array dimensions 5×38.5 mm), designed for laparoscopic use, with nominal center frequency 7 MHz (Vermon LAP-LA). The therapy exposures employed an acoustic power of 18 W with a duty cycle of 63% (4.2 s therapy on, 2.5 s therapy off). B-scans obtained using the laparoscopic imaging probe are shown for for times before treatment and after 2 min treatment. Superimposed on the B-scans are the boundaries of the range window employed for evaluation of attenuation, covering the depth 45–50 mm, distal to the region of ablation. Attenuation caused by the proximal lesion is seen to increase monotonically with treatment time. Similarly increased attenuation can be observed in the third panel of Fig. 2 for an *in vivo* experiment employing a 3 MHz miniaturized image-treat probe.

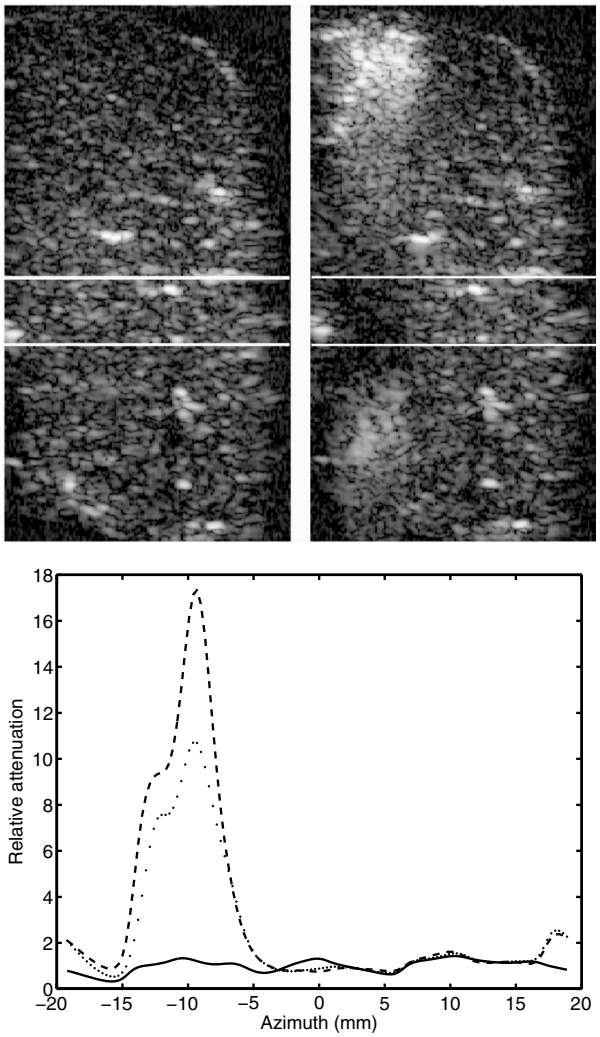

Fig. 3. B-scan images and attenuation maps for of *ex vivo* ablation of porcine liver using a single element, 4.7 MHz therapy transducer and a 7 MHz laparoscopic imaging array. Top: B-scan images before treatment and after 2 min treatment, with superimposed boundaries of window used for attenuation mapping. Each B-scan shows a region of width 38 mm and height 72 mm. Bottom: relative azimuth-dependent attenuation (proportional to inverse of integrated echo energy) immediately (solid line), 1 min (dotted), and 2 min (dashed) after the beginning of thermal treatment.

Fig. 4. Echo difference maps and thermal lesions obtained using a 64 element, 6 MHz image-treat array for two thermal ablation experiments. Each panel shows a region of width 38 mm and height 37 mm. The left and right echo difference images, superimposed on B-scans obtained using the same probes, correspond to the left and right lesions shown in the center panel. The echo difference is displayed by linearly scaling image hue and saturation such that red corresponds to the maximum value and transparency corresponds to the minimum value.

Maps of the echo difference parameter defined above are shown in Fig. 4 for an *ex vivo* treatment using a 64 element image-treat array with a package diameter of 5 mm and a nominal center frequency of 6 MHz. Echo difference maps are superimposed on B-scans obtained using the same probes and compared with cross sections of the thermal lesions in porcine liver. The two lesions shown were obtained by firing 16 elements (sub-aperture size 4.3×9.6 mm) in phase with a frequency of 7.3 MHz, total acoustic power of about 24 W, and an 80% duty cycle (6.0 s therapy, 1.5 s imaging only). The first exposure (left) employed two therapy cycles, while the second exposure (right) employed four therapy cycles. Echo difference maps were obtained using Equation (2) for 32 frames during the imaging portion of each therapy cycle and then cumulatively summed over all therapy cycles. The window employed for spatial integration was a 2D Gaussian function with parameter $\sigma = 1$ mm in both spatial directions. Before computation of the echo difference, an axial motion correction step was implemented by compensation for large-scale phase differences between the analytic echo signals from adjacent frames.

Except for double-image artifacts associated with reverberation between the tissue surface and transducer face, the characteristic shapes and sizes of the echo difference parameter maps correspond well with the lesions. Magnitudes of the echo difference parameter also correspond with the lesion severity, such that the maximum parameter value for the more severe lesion (right) is 17.3, while the maximum for the less severe lesion (left) is 4.2.

An echo difference map obtained during an *in vivo* ablation procedure in porcine liver, using a 16 element, 5.6 MHz, 3 mm image-treat probe, is shown in Fig. 5. For this exposure, all 16 array elements (total aperture size 2.3×12.8 mm) were electronically focused at a depth of 7 mm and fired simultaneously with an approximate acoustic power of 32 W, a total exposure time of 2.3 min, and a 63% duty cycle (4.2 s therapy on, 2.5 s imaging only). Processing was the same as for the *ex vivo* case described above, except that the normalized sum from Eq. (2) was performed over 120 frames during the imaging portion of each therapy cycle and then cumulatively summed over 20 cycles. For comparison, a cross section of the thermal lesion at a depth of 4 mm is also shown. The correspondence between the parametric map and the lesion suggests that this method may be useful for monitoring of thermal ablation *in vivo*, even in the presence of respiration and other tissue motion.

The maximum value for the cumulative, normalized echo difference parameter was 0.02 for the *in vivo* exposure shown and 17.3 for the *ex vivo* exposures shown. Although these values are not directly comparable because of the different transducer geometries and frequencies, their ordering is consistent with the increased lesioning seen for the *ex vivo* exposures illustrated here. However, the large discrepancy may also be due in part to differences between *in vivo* and *ex vivo* tissue, such as the greater gas activity that may be expected in dead tissue.

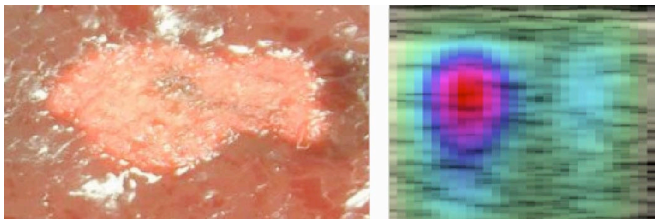

Fig. 5. Echo difference map and thermal lesion for an *in vivo* ablation treatment using a 16 element, 5.6 MHz image-treat probe. Left: cross section of lesion at a 4 mm depth, sliced perpendicular to the image plane. Right: B-scan image with superimposed echo difference map. The echo difference is plotted using the same hue-saturation scale as Fig. 4. The B-scan image/echo difference image has width 13 mm and height 10 mm, while the lesion cross section has width 18 mm and height 10 mm.

IV. Conclusion

Miniaturized dual-functionality (image and treat) ultrasound probes have been successfully used for simultaneous thermal ablation, B-scan imaging, and treatment monitoring.

B-scan image quality is comparable to that achievable using typical transabdominal ultrasound imaging, and is believed to be adequate for thermal ablation planning and guidance. That is, B-scan imaging performed by the miniaturized dual-functionality probes is sufficient to delineate the boundaries between the normal and abnormal tissue, identify critical structures in the vicinity of the target volume, and enables monitoring of the ablation process during treatment.

Monitoring methods including conventional B-scan imaging, attenuation mapping, and analysis of rapid changes in echo signals have potential to effectively guide thermal ablation therapy using image-treat arrays.

References

[1] J. E. Kennedy, G. R. ter Haar, and D. Cranston, "High intensity focused ultrasound: surgery of the future?" Br. J. Radiol. **76**, 590–599 (2003).

[2] S. N. Goldberg, G. S. Gazelle, and P. R. Mueller, "Thermal ablation therapy for focal malignancy: a unified approach to underlying principles, techniques, and diagnostic imaging guidance," Am. J. Roentgenol. **174**, 323–331 (2000).

[3] W. J. Fry, "Biological and medical acoustics," J. Acoust. Soc. Am. **30**, 387–393 (1958).

[4] P. G. Barthe, M. H. Slayton, P. M. Jaeger, I. R. S. Makin, L. A. Gallagher, T. D. Mast, M. M. Runk, and W. Faidi, "Ultrasound therapy system and ablation results utilizing miniature imaging/therapy arrays," 2004 IEEE Ultrasonics Symposium Proceedings.

[5] P. G. Barthe and M. H. Slayton, "Efficient wideband linear arrays for imaging and therapy," 1999 IEEE Ultrasonics Symposium Proceedings, Vol. 2, pp. 1249–1252.

[6] T. D. Mast, W. Faidi, I. R. S. Makin, P. G. Barthe, M. H. Slayton, and V. V. Kouklev, "Method for reducing artifacts in ultrasound imaging," US Patent Application, 2004.

[7] P. S. Green and M. Arditti, "Ultrasonic reflex transmission imaging," Ultrason. Imag. **7**, 201–214 (1985).

[8] L. A. S. Baker and J. C. Bamber, "Performance of reflex transmission imaging (RTI) using a linear array," 2001 IEEE Ultrasonics Symposium Proceedings, Vol. 2, pp. 1551-1554.

[9] T. D. Mast, "Method for monitoring of medical treatment using pulse-echo ultrasound," US Patent Application 20040106870 (2004).

[10] C. Kasai, K. Namekawa, A. Koyano, and R. Omoto, "Real-time two-dimensional blood flow imaging using an autocorrelation technique," IEEE Trans. Son. Ultrason. **32**, 458–464 (1985).

[11] C. J. Hartley, H. Ying, and M. Motomedi, "Ultrasonic Doppler detection of laser-tissue interaction," Ultras. Med. Biol. **20**, 655–663 (1994).